



Room temperature synthesis of graphene-platinum composite as counter electrode for efficient dye-sensitized solar cell

Journal:	<i>RSC Advances</i>
Manuscript ID:	RA-ART-12-2014-016234.R1
Article Type:	Paper
Date Submitted by the Author:	25-Mar-2015
Complete List of Authors:	gao, zhiyong; henan normal university, College of Chemistry and Environmental Science Wang, Lan; Henan Normal University, Liu, Xiao; Henan Normal University, Guo, Peipei; Henan Normal University, Zhao, Wenqi; Henan Normal University, Jiang, kai; henan normal university, School of chemistry and chemical engineering

Cite this: DOI: 10.1039/c0xx00000x

www.rsc.org/xxxxxx

ARTICLE TYPE

Room temperature synthesis of graphene-platinum composite as counter electrode for efficient dye-sensitized solar cell

Zhiyong Gao,^a Lan Wang,^a Xiao Liu,^a Peipei Guo,^a Wenqi Zhao,^a and Kai Jiang^{*a,b}

Received (in XXX, XXX) Xth XXXXXXXXX 20XX, Accepted Xth XXXXXXXXX 20XX

DOI: 10.1039/b000000x

Abstract: Graphene-platinum composites (GPs) with homogeneous decoration of Pt nanoparticles onto graphene sheets were synthesized *via* co-reduction of poly diallyl dimethyl ammonium chloride (PDDA) functionalized graphene oxide and Pt precursor by sodium borohydride (NaBH₄) at room temperature. The photovoltaic performances of the as-prepared GPs as catalytic counter electrodes (CEs) of dye-sensitized solar cells (DSSCs) were examined. By simple modulating of Pt precursor dosage, the homogeneous distribution of Pt nanoparticles onto graphene sheet with a considerable density and a minimal degree of aggregation is achieved, this structural feature is beneficial for improved electrocatalytic activity on I₃⁻ reduction and efficient electrolyte diffusion channel. As a result, a maximal 6.08 % photoelectric conversion efficiency (PCE) of DSSC is achieved based on GP CE, which is 5.71 % higher over that of Pt based counterpart.

Introduction

Ever since the first demonstration of DSSC by O'Regan and Grätzel in 1991 with PCE of 7.9 %, ¹ this neoteric photovoltaic form has attracted extensive research interests for the low fabrication cost, eco-benign process and ever-growing PCE. ²⁻⁴ Generally, a DSSC comprises a dyed TiO₂ photoanode, an I₃⁻/I⁻ redox pair containing electrolyte and a catalytically active Pt CE. Undergoes photo-excitation by sunlight, photoelectrons of dyes are injected to TiO₂ photoanode and transferred rapidly across the film to external circuit to complete electron-hole pairs separation. Whereas the remaining holes in dyes are reduced by I⁻ ions in electrolyte, and the formed I₃⁻ ions then diffuse to Pt CE and subject to catalytic reduction to I⁻ by the accumulated electrons. The readily shuttling of I₃⁻/I⁻ redox pairs between photoanode and CE sustains the recombination of oxidized dyes and eliminates the concentration potential in internal circuit, therefore maintains continuous photoelectric conversion.

For sake of gaining a high PCE, efficient CE with high electrocatalytic activity on I₃⁻ reduction and considerable ions/electrons conductivity are highly required. Pt is currently the most effective CE material for DSSC owing to the excellent electrocatalytic activity and durability on I₃⁻ reduction, as well as the high conductivity. Nevertheless, the expensive and scarce resource of metal Pt contributes significantly to the overall cost of DSSC. Therefore, low Pt and non-Pt materials are significant alternatives to pure Pt for the substantially lower costs. Non-Pt substitute materials, such as carbonaceous materials, ⁵⁻⁹ conductive polymers ¹⁰⁻¹⁴, catalytically active inorganics ¹⁵⁻¹⁸ as well as their composites ^{19,20} are promising CE that can offer comparable PCE to Pt, but the long term stability yet incapable of comparing with Pt. Hence, the low Pt composite is still a class of

competitive CE materials for DSSC. Pure carbon materials including graphene, ²¹⁻²³ carbon black, ²⁴ carbon nanotube, ²⁵⁻²⁷ carbon nanofibers, ^{28,29} have proven to offer acceptable catalytic activity on I₃⁻ reduction, but the PCE of pure carbon based DSSC is relatively lower for the low level of defect sites. ⁷ Albeit this, the generally large surface area, considerable conductivity, and robust chemical inertness against electrolyte make carbon materials ideal matrixes for loading of catalytically active substances to afford composites with optimized conductivity, catalytic activity and stability on I₃⁻ reduction. Amongst the various carbon materials, graphene is highly concerned for the valuable properties such as huge surface areas (up to 2600 m²/g), ⁷ high conductivity and robust chemical stability, all of which are essential feature as supporting for CE active materials of DSSC. ²¹ Given the valuable physicochemical characteristics of graphene and the intrinsically high catalytic activity of Pt on I₃⁻ reduction, GPs were extensively investigated as CEs of DSSCs and demonstrated excellent photovoltaic performance. ^{30,31} As for GPs, the grain size, dispersity and adhesive strength of catalytically active Pt NPs onto graphene should be regulated to afford higher catalytic activity and ions/electrons conductivity, so that the highest PCE can be achieved. In general, the small Pt nanoparticles size means high surface energy, a low synthesis temperature to some extent helps alleviating the sintering or aggregation of Pt nanoparticles from the kinetics viewpoint, thus minimizes the catalytic activity loss. Hence the development of room temperature synthesis route toward GPs is especially meaningful for photovoltaic applications.

In this paper, GPs were synthesized *via* simultaneous reduction of PDDA functionalized graphene oxide and Pt precursor by NaBH₄ at room temperature. Based on the synergistic effect of excellent conductivity and electrocatalytic activity from Pt

nanoparticles and the efficient electrolyte ions and electron transport channel from graphene sheets, photovoltaic performance of DSSC based on the GP CE is apparently improved relative to pure Pt counterpart.

5 Experimental

Synthesis of GPs

Graphene oxide (GO) was synthesized by a modified Hummer's method.^{32,33} The surface modification of GO with PDDA was performed by addition of 2 mL PDDA (40 %) into 50 mL 0.4 mg mL⁻¹ GO suspension under ultrasonication for 1.5 h. The afforded PDDA modified GO was centrifuged and washed repeatedly with distilled water and vacuum dried at 40 °C. To synthesis GPs, 9 mg of PDDA modified GO was dispersed in 25 mL of aqueous solution containing 9, 18, 27 or 36 mg of H₂PtCl₆, and the mixture was ultrasonically treated for 0.5 h to form clear solution. 25 mL of 0.05 M NaBH₄ aqueous solution was then added dropwise into the above mixture under magnetic stirring at ambient temperature to co-reduce GO and Pt precursor. 2 h later, the resulting black solid product was centrifuged and washed repeatedly with deionized water and ethanol and finally dried in a vacuum oven at 40 °C. The obtained products were denoted as GP1, GP2, GP3 and GP4 according to the feeding dosages of Pt precursor.

CEs and DSSC fabrication

To fabricate CEs, 4 mg of G-Pt composite was dispersed in 1 mL ethanol and ultrasonically treated for 30 min to form homogeneous and dilute slurry, which was drop cast directly onto a clean F-doped tin oxide glass substrate (FTO, 14 Ω/cm² NSG, Japan) framed with adhesive tape to control the area and thickness of slurry. Finally, the CE was vacuum dried at 60 °C for electrochemical and photovoltaic measurements. Pt film deposited onto FTO via magnetron sputtering technique was also used for comparison.

TiO₂ photoanode film was fabricated by a similar process. In brief, 4 mg commercial P25 powder (Degussa) and 1 mg hydroxypropyl cellulose (Aldrich) binder were dissolved in 10 mL diethylene glycol under vigorous stirring for 2 h to form viscous paste. The paste was spread onto clean FTO substrate by a traditional doctor blade method with adhesive tape as frame and spacer to control the film thickness to ca. 12 μm, the TiO₂ coated FTO was calcinated at 500 °C for 30 min to remove the organic binder. To improve the connection of P25 NPs, the photoanode was immersed in ice cooled TiCl₄ aqueous solution (0.2 M) and heated at 70 °C for 30 min to coat a thin layer of TiO₂ on surface of P25 particles. The treated film was scratched into 0.25 cm² and calcinated again at 450 °C for 30 min. After being cooled down to 80 °C, the afforded TiO₂ film was sensitized by 0.3 mM cis-bis(isothiocyanato) bis(2,2'-bipyridyl-4,4'-dicarboxylate) Ru (II) bis-tetrabutylammonium dye (N719, Solaronix SA, Switzerland) ethanol solution. The sandwiched DSSCs were fabricated by clamping dyed TiO₂ photoanodes with the abovementioned CEs. An electrolyte containing 0.6 M 1-propyl-3-methylimidazolium iodide (PMII, Geao Co. Ltd, Wuhan), 0.05 M LiI (Lancaster), 0.05 M I₂ (Lancaster), and 0.5 M 4-tert-butylpyridine (New Jersey, USA) in 3-methoxypropionitrile (Lancaster) was injected into the cell *via* capillarity.

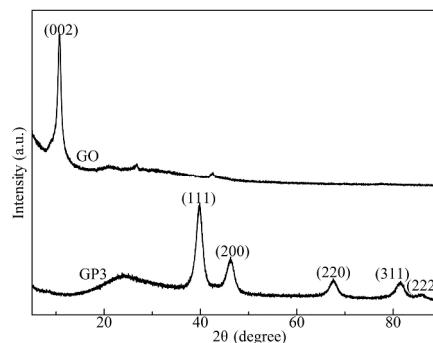


Fig. 1 XRD patterns of GO and GP3.

Characterizations and electrochemical tests

The microstructures and components of the samples were characterized by high resolution transmission electronic microscopy (HRTEM, JEOL JEM-2100) and X-ray powder diffraction (XRD, Bruker D8 Advance with Cu Kα radiation), X-ray photoelectron spectroscopy (XPS, ThermalFisher ESCALab 250 X-ray photoelectron spectrometer with Al Kα radiation), Raman spectroscopy (JOBIN YVON HR800 Confocal Raman spectrometer with 632.8 nm laser excitation) and thermogravimetric analysis (TGA, Netzsch STA 449C analyzer). Cyclic voltammograms (CVs) and Tafel polarization curves of the CEs were measured on a CHI 660D electrochemical workstation (Chenhua, Shanghai). In cyclic voltammetry measurements, the three-electrode test system includes a Pt wire auxiliary electrode, a Ag/AgCl reference electrode and a GP working electrode immersed in acetonitrile electrolyte containing 10 mM LiI, 1 mM I₂ and 0.1 M LiClO₄ with potential scan rate of 50 mV/s. Tafel polarization curves of the symmetric cells composing of two identical CEs were measured in double-electrode configuration. Electrochemical impedance spectroscopy (EIS, EG&G M283) was also measured in symmetric double-electrode configuration at zero bias potential and 10 mV amplitude over the frequency range 0.01-10⁵ Hz. Electrochemical active surface areas (ESAs) of GPs were estimated from hydrogen electrosorption CVs, which were recorded between -0.2 and 1.2 V in 0.5 M N₂ saturated H₂SO₄ solution. Photocurrent-voltage (*J-V*) curves of the DSSCs based on various CEs were measured on a Keithley 2400 sourcemeter under the illumination of a xenon lamp solar simulator (Newport) with incident light intensity of 100 mW/cm² (AM 1.5).

Results and discussion

Morphological and structural characterizations

Fig. 1 shows the XRD patterns of GO and GP3. As for GO, a significant (002) peak appears at $2\theta = 10.4^\circ$, which corresponds to a d-spacing of 0.83 nm. The dramatically larger interlayer distance of the GO relative to graphite is associated with the oxygen containing groups such as hydroxyl, epoxy, and carboxyl groups on the basal plane and border of graphene sheet.^{33,34} These surface functional groups offer essential hydrophilic of GO and favor the aqueous solution processable preparation of graphene based composite. Moreover, the functional groups act as chelating ligands assisting the homogeneous immobilization of the formed Pt nanoparticles onto graphene sheets free from

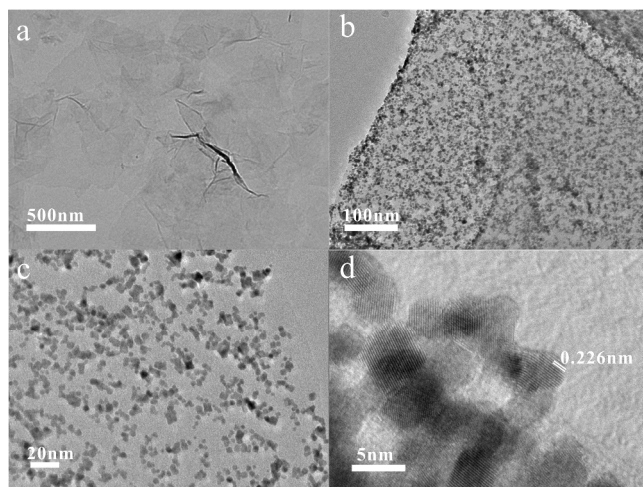


Fig. 2 TEM of (a) PDDA modified GO and (b-d) GP3.

aggregation. As for GPs, the disappearance of (002) facet diffraction of GO and the appearance of a wide peak at 25° indicate the reduction of GO to graphene by NaBH_4 .³⁵ In addition, the diffraction peaks at 39.8 , 46.2 , 67.6 , 81.5 and 85.9° are in turn assigned to the reflection of (111), (200), (220), (311) and (222) crystallographic planes of face-centered cubic phased Pt.³⁵ All of these diffraction peaks evidence the simultaneous reduction of platinum precursor and GO by NaBH_4 . The wide diffraction peaks of Pt suggest the tiny size of the formed Pt nanoparticles in GPs.

Fig. 2 presents the TEM images of PDDA modified GO and GP3. From Fig. 2a, PDDA modified GO demonstrates transparent two-dimensional sheet-like outline with silk veil waves, which is typical feature of single or several layered GO sheet with flexible texture owing to the one atom layer thickness of GO and the aggregation at some regions. Fig. 2b shows the TEM image of GP3, it is clear that Pt nanoparticles with size of 4~6 nm are homogeneously scattered on graphene sheets at a high density. Magnified image (Fig. 2c) reveals that the Pt nanoparticles are homogeneous decorated onto graphene sheet with a minimal aggregation, the largely isolated nanoparticles is beneficial for high catalytic activity because of the higher surface utilization ratio of catalytically active Pt. The well dispersity of Pt nanoparticles is presumably due to the structure characteristics of PDDA modified GO, the positive charge of PDDA make it well adsorbed onto GO sheet *via* non-valence interaction, which results in the positively charged surface of modified GO, thus benefits the firmly and homogeneously anchoring of Pt precursor *via* polar interactions. Moreover, the interfacial oxygen containing groups onto GO sheet also help anchoring of Pt precursors *via* hydrogen bonds or polar interactions. As a consequence, the formed Pt particles by NaBH_4 reduction can be well distributed onto graphene sheet without severe aggregation. Meanwhile, the oxygen containing groups are also removed simultaneously by NaBH_4 reduction, restoring the hexagonal sp^2 hybrid lattice and conductivity of graphene. Li *et al* had reported that the noble metal Pd can interact with graphitic carbon skeleton *via* coordination interactions,³⁶ it is presumably Pt nanoparticles may also be tightly anchored onto graphene framework *via* the similar manner. The strong interaction

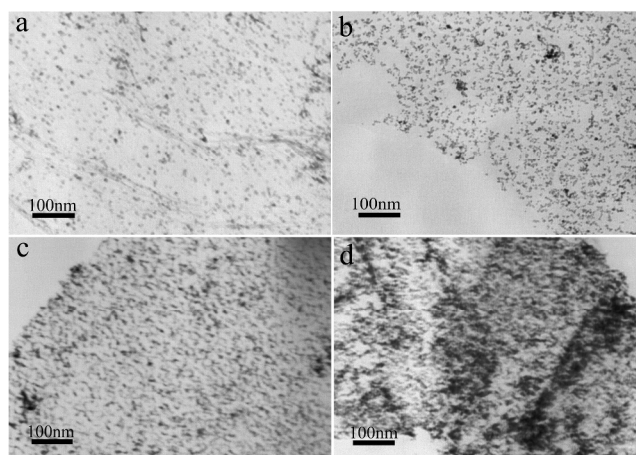


Fig. 3 TEM of (a) GP1, (b) GP2, (c) GP3, and (d) GP4.

between Pt nanoparticles and graphene is significant for decreasing the overall surface energy of Pt nanoparticles and attenuates their aggregation. Moreover, the tight attachment of Pt nanoparticles onto graphene also favors a higher interface conductive connection between them, which will lead to a lower inner resistance. On the other hand, the immobilized Pt nanoparticles onto graphene can function as a spacer alleviating the restacking of graphene sheets and provide efficient electrolyte diffusion channel to access to Pt sites. All of these factors are beneficial for a high catalytic activity for I_3^- reduction. Fig. 2d shows the HRTEM images of GP3, Pt nanoparticles with size of *ca.* 5 nm were distributed onto graphene sheet with a fine density, clear lattice fringes with a lattice spacing of 0.226 nm can be observed, which corresponds to (111) planes of the face-centered cubic Pt,³⁷ suggesting the effective formation of Pt nanoparticles by NaBH_4 reduction.

Fig. 3 presents the TEM images of GPs synthesized with different H_2PtCl_6 dosages. It can be observed that the size of Pt nanoparticles almost not vary with the Pt precursor dosage, whereas the density increases from GP1 to GP4. In GP1 and GP2 (Fig. 3a-b), the Pt nanoparticles are well dispersed onto graphene sheet with relatively lower density, the increase of Pt precursor dosage mainly results in higher density of Pt nanoparticles, simultaneously, slight aggregation of Pt nanoparticles gradually occurs (Fig. 2b-c, and Fig.3c). The further increment in Pt precursor dosage causes the severe aggregation of Pt nanoparticles, from Fig. 3d, the formed Pt nanoparticles aggregate heavily on graphene in GP4, which is not advantageous for catalysis application considering the less efficient utilization ratio of noble metal Pt. All of the TEM images reveal that PDDA can function as anchor sites facilitating the nucleation and growth of Pt nanoparticles onto graphene surface and constrains their aggregation. At lower PtCl_6^{2-} concentration, the precursors are confined by the sufficient positively charged PDDA *via* electrostatic interaction and function as nucleation center for the growth of the formed Pt, preventing the aggregation of Pt nanoparticles,³⁸ thus results in the homogeneous scattering of Pt nanoparticles onto graphene sheet with low density. While at higher initial PtCl_6^{2-} concentration, the PDDA functionalities available for Pt gradually saturates, so the inevitable aggregation of Pt nanoparticles occurs. Simultaneously, GO can also be

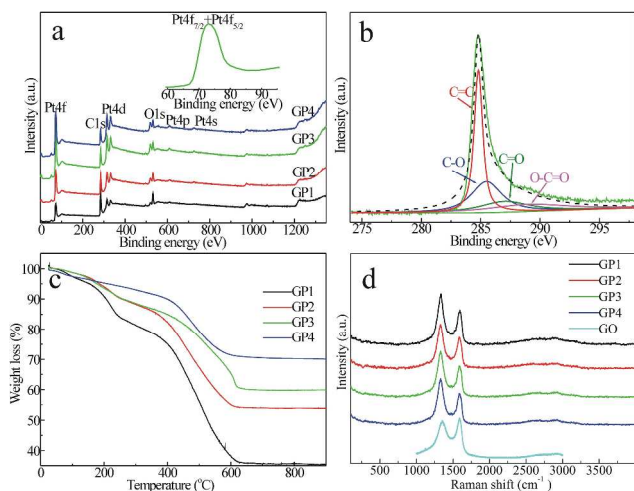


Fig. 4 (a) XPS survey spectra of GPs, inset: detailed Pt4f spectrum. (b) Deconvoluted XPS C1s spectrum of GP3. (c) TGA of GPs in air atmosphere, (d) Raman spectra of GPs and GO.

reduced by NaBH_4 , forming GPs with controlled immobilization density of Pt nanoparticles onto graphene. In order to gain efficient and economic GPs CE materials, Pt precursor dosage should be well controlled to optimize the density of the catalytically active Pt nanoparticles on graphene sheet.

The surface chemical composition of GPs are characterized by XPS, from Fig. 4a, all the samples comprise C, O and Pt elements, the similar peak positions indicate the same compositions in GPs. To be noted, the intensity of Pt peaks increases from GP1 to GP4, indicating the gradually increment in Pt content. High resolution Pt4f spectrum (Inset) shows a broad band centered at 72.9 eV, which is the superimposition of Pt4f_{7/2} (71.3 eV) and Pt4f_{5/2} (74.5 eV) spin-orbits of zero valent Pt,³⁹ suggesting the formation metallic Pt. Deconvolution of C1s peak (Fig. 4b) shows the presence of C=C (284.6 eV), C-O (285.5 eV), C=O (287.4 eV) and O-C=O (289.5 eV) bonds, the overwhelming C=C bond validates the efficient reduction of GO. Both Pt4f and C1s XPS peaks evidence the co-reduction of Pt precursor and GO by NaBH_4 . From the atomic ratio of Pt, the surface mass percentage of Pt are 45, 61, 70 and 88 %, respectively for GP1~GP4. Pt contents in GPs were also estimated by TGA measurements in air atmosphere *via* burning off graphene and functional groups. As shown in Fig. 4c, all samples show similar trend in TG curves, the slight mass loss below 100 °C is attributed to the evaporation of adsorbed moisture in composites. Another weight loss in temperature range of 200~280 °C is presumably associated with the elimination of volatile functional groups on graphene motif. The prominent weight loss at 400~620 °C can be attributed to the combustion of graphene framework. The mass percentage of Pt were estimated to be 35, 54, 60 and 70 wt%, respectively in GP1~GP4, indicating the increment in Pt content for the GPs when more Pt precursor is used in synthesis procedure. Relative to TGA results, the apparently higher Pt percentages calculated from XPS analyses mainly lies in the coating of Pt nanoparticles onto graphene sheets, thus results in the relatively higher surface Pt content than the overall composition. Raman spectra of GPs (Fig. 4c) display two distinct vibration peaks at about 1336 (D-band) and 1595 cm^{-1} (G-band), the former one is attributed to the A_{1g} vibration of structural

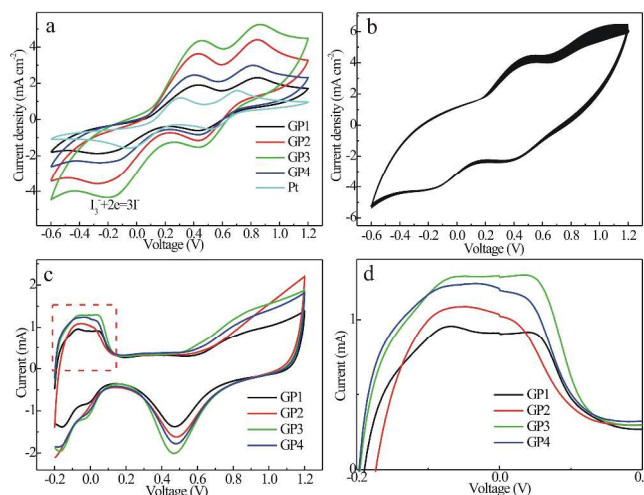


Fig. 5 (a) CVs of Pt and GPs electrodes at a scan rate of 50 mV s^{-1} in acetonitrile electrolyte containing 10 mM LiI, 1 mM I₂, and 0.1 M LiClO₄ at a scan rate of 50 mV/s. (b) Consecutive 500 cycles of CVs at GP3 electrode with scan rate of 50 mV s^{-1} . (c,d) CVs of GPs electrodes in N₂ saturated 0.5 M H₂SO₄ at a scan rate of 50 mV s^{-1} .

defects or partially disordered structure in sp² carbon domains, whereas the latter is associated with the E_{2g} symmetric vibration mode of sp² graphitic carbon framework. The D-band to G-band intensity ratio (I_D/I_G) reflects the degree of defect lattices and structural disorder in carbon materials. I_D/I_G of GPs ranges within 1.19~1.24, which are higher over that of GO (0.82), showing the generation of many structural defects on graphene framework during reduction reaction.

Electrochemical characteristics

Catalytic reduction of I₃⁻ is the main role of CE, to evaluate the electrocatalytic activity of GPs on this reaction, CVs of Pt and GPs were compared at first (Fig. 5a). Two pairs of reversible redox peaks are visualized in CVs, which are attributed to the redox conversions between I₃⁻/I⁻ and I₂/I₃⁻ pairs.⁴⁰ The cathodic peak at *ca.* -0.18 V is caused by the reaction: I₃⁻ + 2e = 3I⁻. The produced I⁻ by this reaction ensures the regeneration of oxidized dyes, which directly affects the photovoltaic performance of DSSCs. It can be observed that current density of pure Pt electrode is relatively low, which may be due to the mirror-like Pt electrode with little roughness can only offer limited contact area for I₃⁻ ions, the low surface utilization ratio results in the low catalytic activity. In contrast, the current densities of GPs are apparently higher over Pt electrode, indicating the enhanced catalytic activity on I₃⁻ reduction, which may be caused by the well distribution of Pt nanoparticles onto graphene sheet, thus offer increased surface utilization ratios. Additionally, the high surface area of graphene also contributes to the higher accessible surface areas of GPs, which can be evidenced from the enhanced capacitive current or the area encircled within CVs. As for GPs electrodes, catalytic current increases correspondingly with Pt content from GP1 to GP3, which may be ascribed to the increased density of Pt nanoparticles with similar size, the higher content of Pt provides more active sites for I₃⁻ reduction. Besides, the high content of Pt nanoparticles onto graphene alleviates the face to face stack or aggregation of graphene and avoids the enwrapping of Pt nanoparticles into graphene sheets, maintaining a high level

of exposed Pt sites to electrolyte and resulting in improved catalytic activity. Although the defect sites of graphene can also catalyze I_3^- reduction and function solely as CE of DSSC, the catalytic activity in our case is rather low, the catalytic activity herein is predominantly derived from Pt nanoparticles. With the increase of Pt content to 60 %, GP3 offers the highest catalytic activity, the reduction current is 2.5 times higher than that of Pt electrode. Further increases of Pt content deteriorate the catalytic activity, as for GP4, the catalytic current decreases sharply, which associates with the lowered surface utilization ratio of Pt for the severe aggregation. The inefficient usage of Pt nanoparticles also causes waste in cost. In view of the highest catalytic activity and the thrifty in utilization of Pt, GP3 is the most suitable catalytic CE material for DSSC. The catalytic durability of GP3 is also measured, as shown in Fig. 5b, after 500 cycles of consecutive CV measurements, the catalytic current for I_3^- reduction almost not varies, showing excellent catalytic durability. The excellent catalytic durability is attributed to the robust structural stability of GP3, which is vital for enduring the long term application of pertinent DSSC.⁴¹ Based on these CV features, it can be preliminarily concluded that GP3 is an efficient CE materials for DSSC owing to the high catalytic activity and durability.

Since the catalytic activity is dependent on the accessible surface sites of catalyst, ESAs of GPs were examined to figure out the enhanced electrocatalytic activity of the GPs. ESAs of GPs can be acquired by CV measurements in 0.5 H₂SO₄ electrolyte. From Fig. 5c-d, CVs of GPs all show a pair of cathodic/anodic peaks within -0.2~0.10 V, which represent the adsorption and desorption of atomic hydrogen on Pt surface in acidic media.^{35,38} The integrated areas under desorption peaks in CVs reflect coulombic charge involved in hydrogen desorption under the assumption that a value of 210 $\mu\text{C cm}^{-2}$ for the desorption of a hydrogen monolayer. ESAs of GPs were estimated according to Eq. 1:⁴²

$$\text{ESA} = Q_H / (210 m_{\text{Pt}}), \quad (1)$$

Where Q_H ($\mu\text{C cm}^{-2}$) is the coulombic charge associate with hydrogen desorption or adsorption, m_{Pt} (g cm^{-2}) is the Pt loading amount. Our calculation results show that ESAs of GP1, GP2, GP3 and GP4 are 50.4, 52.3, 75.4 and 67.3 $\text{cm}^2 \text{g}^{-1}$, respectively. The high ESAs originate from the highly exposed Pt atoms to electrolyte and would be responsible for the high electrocatalytic activities. The increase of ESA from GP1 to GP3 is mainly due to the higher density of Pt nanoparticles onto graphene, which alleviate the ratio of enwrapped Pt. Whereas the value decreases with further increment in Pt content, which may be due to the severe aggregation of Pt nanoparticles, the decreased utilization ratio of Pt finally causes the less active sites and the deterioration in catalytic activity.

To gain further insight into the interfacial electrochemical behavior on catalytic CE, EIS of symmetric CE based on GPs and Pt electrode were measured and shown in Fig. 6a. Generally, in Nyquist plots of EIS, CE related impedance mainly includes intrinsic series resistance of CE (R_s , located at high frequency of ~100 kHz), charge transfer resistance at CE/electrolyte interface (R_{ct} , intermediate frequency of 1-100 kHz) and Warburg diffusion impedance of electrolyte (Z_w , low frequency range of 0.1-10 Hz).^{40,43,44} Herein, the Nyquist plots of all cells show two arcs (Fig. 6a), by fitting the plots using the equivalent circuit in inset,

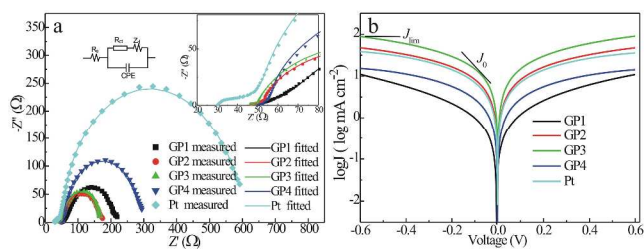


Fig. 6 (a) Nyquist plots and (b) Tafel polarization curves of symmetrical cells based on different electrodes. Inset in panel (a): equivalent circuit and enlarged EIS plots at high frequency region.

R_s of GPs (47.9~53.4 $\Omega \text{ cm}^2$) are larger than Pt device (32.1 $\Omega \text{ cm}^2$), which may be due to the intrinsically lower conductivity of chemically reduced graphene and the less compatibility of GPs films to FTO substrate relative metal Pt, as well as the less effective electrons propagation channel in the loose texture of GPs. In contrast, from inset, R_{ct} of GPs electrodes (2.1~8.8 $\Omega \text{ cm}^2$) are lower than Pt electrode (11.0 $\Omega \text{ cm}^2$), this trend is attributed to the more accessible active sites and therefore higher catalytic activity on I_3^- reduction, which is evidenced by CV results. Amongst the GPs electrodes, the lowest R_{ct} (2.1 $\Omega \text{ cm}^2$) is achieved for GP3, suggesting the highest catalytic activity, which may be derived from the homogeneous decoration of Pt nanoparticles onto graphene sheet with high density free of aggregation, thus allows sufficient contact between Pt nanoparticles and electrolyte, producing more Γ for dyes regeneration and further the efficient light capturing and photoelectrons injection process, ensuring a higher short circuit current density (J_{sc}) for the pertinent DSSC. Most notably, from the diameter of the arcs at low frequency region, Z_w for GPs devices (109.7~232.1 $\Omega \text{ cm}^2$) are substantially lower than Pt counterpart (543 $\Omega \text{ cm}^2$), this large difference indicates that Z_w in this case is the major parameter determining the inner circuit resistance of CE. Porous GPs texture with immobilized Pt nanoparticles spacer between graphene sheets is highly required for electrolyte ions diffusion.

To further elucidate the electrocatalytic activity of CEs on I_3^-/Γ exchange, Tafel polarization curves of the symmetric cells were measured. Fig. 6b presents the logarithmic current density ($\log J$) as a function of polar potential (U) for I_3^- reduction. In the polarization zone at low potential region, the slope of GP3 electrode is the highest one, implying the highest exchange current density (J_0), which reflects the highest catalytic activity.⁴⁵⁻⁴⁷ Meanwhile, J_0 can also be evaluated from R_{ct} in EIS according to Eq. (2).⁴⁵

$$J_0 = RT/nFR_{ct} \quad (2)$$

Where R is the gas constant, T is the absolute temperature, F is the Faraday constant, and n is the number of electrons involved in the reduction of I_3^- to Γ . According to this inverse proportion relationship between J_0 and R_{ct} , the trend of J_0 for GPs and Pt electrodes obtained from EIS basically coincides with that from Tafel polarization measurement. The higher J_0 of GP2 and GP3 manifest their superior electrocatalytic activities from another perspective, which coincide with CV data (Fig. 5a). Additionally, limiting diffusion current density (J_{lim}) can be obtained from the current density at high potential end, which depends on the

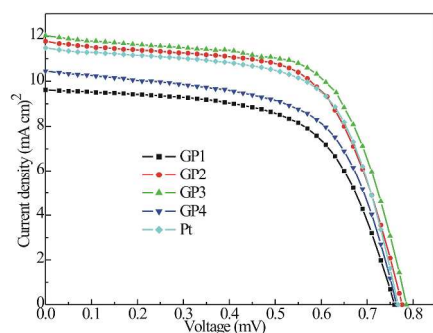


Fig. 7 J - V curves of DSSCs based on different CEs.

diffusion coefficient of I_3^-/I^- pairs in electrolyte.^{46,47} The diffusion coefficient (D) of electrolyte is in linear with J_{lim} based on Eq. (3):

$$D = lJ_{lim}/2nFC \quad (3)$$

Where l is the spacer thickness, C is the concentration of I_3^- . J_{lim} of GP2 and GP3 are higher over Pt electrode, indicating the superior D of the two composites. The high J_{lim} is attributed to the considerable density of Pt onto graphene sheet, the efficient electrolyte diffusion channel between adjacent graphene sheets accelerates the electrolyte diffusion and allows more efficient inner circuit charge exchange.

Photovoltaic performances

The high catalytic activity on I_3^- reduction makes GPs efficient CE materials of DSSC. Fig. 7 showed the J - V curves of the DSSCs based on sputtered Pt and GPs CEs. The DSSC based on sputtered Pt CE offers a J_{sc} of 11.48 mA cm^{-2} , an open circuit voltage (V_{oc}) of 0.77 V, and a FF of 0.65, which result in a PCE of 5.71 %. The photocurrents of GPs based cells differ apparently, mainly due to the highest catalytic activity on I_3^- reduction, J_{sc} of GP3 based cell increased to 12.03 mA cm^{-2} , and V_{oc} also slightly increased to 0.79 V, whereas FF maintains a high level as Pt based cell, which results in a PCE of 6.08 %. The higher J_{sc} and V_{oc} are indirectly related to the high catalytic activity of GP3 on I_3^- reduction, thus produces more I^- for dyes regeneration and further results in more efficient light harvesting and electrons injection to conduction band of TiO_2 photoanode, *viz.* a higher J_{sc} . Meanwhile, more photoelectrons at TiO_2 conduction band elevates the Fermi level of TiO_2 photoanode, thus leads to a wider gap between CE and photoanode, *viz.* a higher V_{oc} . Moreover, the lower overpotential of GP3 on I_3^- reduction also contributes to the enhanced V_{oc} , so the higher voltage is also reasonable. Compared with GP3 based cell, J_{sc} and V_{oc} of GP2 based cell both slightly decrease, which is due to the lower catalytic activity on I_3^- reduction. Additionally, FF also decreases for the same reason, as a result, PCE of GP2 lowers to 5.76 %, but the value is still slightly higher over pure Pt based cell. This trend is basically in accordance with the CV result. As for the cells based on GP1 and GP4 CEs, all the photovoltaic parameters are inferior to GP3 based cell because of the lower catalytic activities. In this sense, the Pt content in the composite should be optimized for sake of gaining higher PCE. Too high fraction of noble metal Pt is not necessarily favorable for higher PCE. Besides, the relatively high cost is also not appropriate for application as CE of DSSC. Due to the excellent catalytic activity and durability, as well as the 40 %

lowered utilization amount of noble metal Pt, GP3 is our work is an efficient and economic CE material for DSSC.

Conclusions

In summary, GPs were synthesized by co-reduction of PDDA functionalized GO and Pt precursor with $NaBH_4$ at room temperature. The different Pt content results in the enhanced electrocatalytic activity for I_3^- reduction to different extents. Due to the highest catalytic activity and durability, the lowered resistance at CE/electrolyte interface and the thrifty in Pt utilization dosage, the DSSC based on GP3 well balances the cost and PCE and therefore can be deemed as optimal CE for DSSC.

Acknowledgments:

This work was supported by National Science Foundation of China (Nos. 61204078, 61176004, U1304505), Program for Innovative Research Team and Talent (in Science and Technology) in University of Henan Province (Nos. 13IRTSTHN026, 15HASTIT006), Key Project of Science and Technology of Henan Province (No. 122102210561) and the Key Project of Science and Technology of Xinxiang City.

Notes and references

- ^a School of Chemistry and Chemical Engineering, Henan Normal University, Xinxiang, 453007, China.
- ^b Collaborative Innovation Center of Henan Province for Green Manufacturing of Fine Chemicals, Key Laboratory of Green Chemical Media and Reactions, Ministry of Education, Henan Normal University, Xinxiang, 453007, China. E-mail: kjiang512@163.com.
- 1 B. O'regan and M. Grätzel, *Nature*, 1991, **353**, 737–740.
- 2 M. Grätzel, *Nature*, 2001, **414**, 338–344.
- 3 A. Yella, H.W. Lee, H.N. Tsao, C. Yi, A.K. Chandiran, M. Nazeeruddin, E.W. Diau, C.Y. Yeh, S.M. Zakeeruddin, M. Grätzel, *Science*, 2011, **334**, 629–634.
- 4 H.J. Ahn, I.H. Kim, J.C. Yoon, S.I. Kim and J.H. Jang, *Chem. Commun.*, 2014, **50**, 2412–2415.
- 5 W. Kwon, J.M. Kim, S.W. Rhee, *J. Mater. Chem. A*, 2013, **1**, 3202–3215.
- 6 A. KumaráJena, *Energy Environ. Sci.*, 2012, **5**, 7001–7006.
- 7 P. Poudel and Q.Q. Qiao, *Nano Energy*, 2014, **4**, 157–175.
- 8 S. Thomas, T.G. Deepak, G.S. Anjusree, T.A. Arun, S.V. Nair and A.S. Nair, *J. Mater. Chem. A*, 2014, **2**, 4474–4490.
- 9 H.X. Xu, C.J. Zhang, Z.W. Wang, S.P. Pang, X.H. Zhou, Z.Y. Zhang and G.L. Cui, *J. Mater. Chem. A*, 2014, **2**, 4676–4681.
- 10 C. Bu, Q. Tai, Y. Liu, S. Guo and X. Zhao, *J. Power Sources*, 2013, **221**, 78–83.
- 11 B.L. He, Q.W. Tang, J.H. Luo, Q.H. Li, X.X. Chen and H.Y. Cai, *J. Power Sources*, 2014, **256**, 170–177.
- 12 Q.W. Tang, H.Y. Cai, S.S. Yuan, X. Wang, *J. Mater. Chem. A*, 2013, **1**, 317–323.
- 13 J.H. Wu, Q.H. Li, L.Q. Fan, Z. Lan, P.J. Li, J.M. Lin, S.C. Hao, *J. Power Sources*, 2008, **181**, 172–176.
- 14 H. Wang, Q. Feng, F. Gong, Y. Li, G. Zhou and Z.S. Wang, *J. Mater. Chem. A*, 2013, **1**, 97–104.
- 15 H.C. Sun, D. Qin, S.Q. Huang, X.Z. Guo, D.M. Li, Y.H. Luo, Q.B. Meng, *Energy Environ. Sci.*, 2011, **4**, 2630–2637.
- 16 X.K. Xin, M. He, W. Han, J.H. Jung, Z.Q. Lin, *Angew. Chem. Int. Ed.*, 2011, **50**, 11739–11742.
- 17 M.X. Wu, X. Lin, Y.D. Wang, L. Wang, W. Guo, D.D. Qu, X.J. Peng, A. Hagfeldt, M. Grätzel, T.L. Ma, *J. Am. Chem. Soc.*, 2012, **134**, 3419–3428.
- 18 F. Gong, X. Xu, Z.Q. Li, G. Zhou, Z.S. Wang, *Chem. Commun.*, 2013, **49**, 1437–1439.
- 19 W.W. Sun, T. Peng, Y.M. Liu, S. Xu, J.K. Yuan, S.S. Guo, X.Z. Zhao, *J. Mater. Chem. A*, 2013, **1**, 2762–2768.

- 20 W.W. Sun, T. Peng, Y.M. Liu, N. Huang, S.S. Guo, X.Z. Zhao, *Carbon*, 2014, **77**, 18–24.
- 21 H. Wang, Y.H. Hu, *Energy Environ. Sci.*, 2012, **5**, 8182–8188.
- 22 J.D. Roy-Mayhew, D.J. Bozym, C. Punckt, I.A. Aksay, *ACS Nano*, 2010, **4**, 6203–6211.
- 23 X. Pan, K. Zhu, G.F. Ren, N. Islam, J. Warzywoda, Z.Y. Fan, *J. Mater. Chem. A*, 2014, **2**, 12746–12753.
- 24 T. N. Murakami, S. Ito, Q. Wang, M. K. Nazeeruddin, T. Bessho, I. Cesar, P. Liska, R. H. Baker, P. Comte, P. Pechy and M. Gratzel, *J. Electrochem. Soc.*, 2006, **153**, A2255.
- 25 X. Mei, S.J. Cho, B.Fan, J.Ouyang, *Nanotechnology*, 2010, **21**, 395202.
- 26 K.T. Dembele, R. Nechache, L. Nikolova, A. Vomiero, C. Santato, S. Licoccia, F. Rosei, *J. Power Sources*, 2013, **233**, 93–97.
- 27 S.Q. Huang, Z.B. Yang, L.L. Zhang, R.X. He, T. Chen, Z.B. Cai, Y.F. Luo, H.J. Lin, H. Cao, X.R. Zhu, H.S. Peng, *J. Mater. Chem.*, 2012, **22**, 16833–16838.
- 28 P. Joshi, L.F. Zhang, Q.L. Chen, D. Galipeau, H. Fong, Q.Q. Qiao, *ACS Appl. Mater. Interf.*, 2010, **2**, 3572–3577.
- 29 G. Veerappan, W. Kwon, S.W. Rhee, *J. Power Sources*, 2011, **196**, 10798–10805.
- 30 G.T. Yue, J.H. Wu, Y.M. Xiao, M.L. Huang, J.M. Lin, L.Q. Fan and Z. Lan, *Electrochim. Acta*, 2013, **92**, 64–70.
- 31 V.D. Dao, L.V. Nang, E.T. Kim, J.K. Lee and H.S. Choi, *ChemSusChem*, 2013, **6**, 1316–1319.
- 32 C. Nethravathi and M. Rajamathi, *Carbon*, 2008, **46**, 1994–1998.
- 33 Z.Y. Gao, N. Liu, D.P. Wu, W.G. Tao, F. Xu and K. Jiang, *Appl. Surf. Sci.*, 2012, **258**, 2473–2478.
- 34 H.K. Jeong, M.H. Jin, K.H. An and Y.H. Lee, *J. Phys. Chem. C*, 2009, **113**, 13060–13064.
- 35 S. Sharma, A. Ganguly, P. Papakonstantinou, X. Miao, M. Li, J.L. Hutchison, M. Delichatsios and S. Ukleja, *J. Phys. Chem. C*, 2010, **114**, 19459–19466.
- 36 X. Yan, Q.Q. Li, L.S. Li, *J. Am. Chem. Soc.*, 2012, **134**, 16095–16098.
- 37 Y. Li, L. Tang and J. Li, *Electrochem. Commun.*, 2009, **11**, 846–849.
- 38 Y. Xing, *J. Phys. Chem. B*, 2004, **108**, 19255–19259.
- 39 C.S. Liu, X.C. Liu, G.C. Wang, R.P. Liang, J.D. Qiu, *J. Electroanal. Chem.*, 2014, **728**, 41–50.
- 40 X.L. Duan, Z.Y. Gao, J.L. Chang, D.P. Wu, P.F. Ma, J.J. He, F. Xu, S.Y. Gao and K. Jiang, *Electrochim. Acta*, 2013, **114**, 173–179.
- 41 J.H. Wu, Z.Y. Tang, Y.F. Huang, M.L. Huang, H.J. Yu and J.M. Lin, *J. Power Sources*, 2014, **257**, 84–89.
- 42 Y.J. Li, W. Gao, L.J. Ci, C.M. Wang, P.M. Ajayan, *Carbon*, 2010, **48**, 1124–1130.
- 43 A. Hauch, A. Georg, *Electrochim. Acta*, 2001, **46**, 3457–3466.
- 44 H.C. Sun, Y.H. Luo, Y.D. Zhang, D.M. Li, Z.X. Yu, K.X. Li, Q.B. Meng, *J. Phys. Chem. C*, 2010, **114**, 11673–11679.
- 45 M.X. Wu, Q.Y. Zhang, J.Q. Xiao, C.Y. Ma, X. Lin, C.Y. Miao, Y.J. He, Y.R. Gao, A. Hagfeldt, T.L. Ma, *J. Mater. Chem.*, 2011, **21**, 10761–10766.
- 46 M.X. Wu, X. Lin, A. Hagfeldt, T.L. Ma, *Chem. Commun.*, 2011, **47**, 4535–4537.
- 47 C.J. Liu, S.Y. Tai, S.W. Chou, Y.C. Yu, K.D. Chang, S. Wang, F.S.S. Chien, J.Y. Lin, T.W. Lin, *J. Mater. Chem.*, 2012, **22**, 21057–21064.